Boundary-layer flow in a porous domain above a flat plate

Miltiadis V. Papalexandris[1]

[1]Institute of Mechanics, Materials and Civil Engineering, Université catholique de Louvain, Louvain-la-Neuve, 1348, Belgium.

Contributing authors: miltos.uclouvain.be;

Abstract

This paper is concerned with the structure and properties of boundary-layer flow in a porous domain above a flat plate. The flow is generated by an incoming uniform stream at the vertical boundary of the porous domain and is maintained by an external pressure forcing. Herein we provide the parametrization of the interphasial drag in terms of a Darcy-Forchheimer law, derive the momentum boundary-layer equation and elaborate on the profile of the free-stream velocity. The boundary-layer equation is then solved numerically via the local similarity method and via two local nonsimilarity methods at different levels of truncation. The accuracy of these methods is compared via a series of numerical tests. For the problem in hand, the free-stream velocity decreases monotonically to a terminal far-field value. Once this value is reached, the velocity profile no longer evolves in the streamwise direction. The computations further reveal that, for sufficiently small external forcing, the boundary-layer thickness initially increases, reaches a peak and then decreases towards its terminal value. This unusual overshoot is attributed to the large variation of the rate of decrease of the free-stream velocity. On the other hand, our computations predict that the wall stress always decreases monotonically in the streamwise direction.

Keywords: nonsimilar boundary layers, porous media, local nonsimilarity method, Riccati equation, Darcy-Forchheimer law.

MSC Classification: 76D10 , 76S05 , 76M45

1 Introduction

Boundary-layer theory constitutes a well established perturbation method for obtaining approximate solutions to boundary-value problems in domains with solid boundaries or interfaces. Thus far, it has been extensively applied in such problems arising in fluid dynamics, heat transfer [1], and other branches of mechanics. With regard to porous-media flows, it has been applied mostly in thermal boundary layers in unbounded and bounded domains. Examples of application are natural of forced convection over plates, flows around solid bodies, forced convection in porous channels, natural convection in porous enclosures, and many others. The literature on these topics is quite extensive; for a detailed account, the interested reader is referred to [2] and references therein.

The study of the hydrodynamic boundary layers in porous domains has also been the topic of several studies in the past, mainly in the context of forced convection over a plate. For example, Vafai & Tien [3] performed a numerical analysis of the hydrodynamic and thermal layers over a flat plate. For the same problem, Vafai & Thiyagaraja [4] examined the structure of the boundary layers on the basis of an asymptotic power-series in terms of the porosity. However, in the studies [3, 4], the advective term of the momentum equation had been neglected. The full boundary-layer momentum equation (including the nonlinear advective term) was studied by Nakayama et al. [5] who provided numerical solutions based on the local similarity solution method [6]. This study was later extended by Hossain et al. [7] to flows over a wedge embedded in a porous medium. More recently, boundary layers in forced convection of Casson fluid, which is shear-thinning, over a plate embedded in a porous medium have been analysed in [8–10] via the local nonsimilarity method.

However, in all of the afore-mentioned works it was assumed that the solid body, flat plate or wedge, is embedded in the porous medium. In other words, the porous medium covered the space not only above but also upstream of the solid body. Accordingly, the free-stream velocity (i.e. the velocity outside the boundary layer) is uniform, which amounts to a considerable reduction of the complexity of the governing equations. Actually, in the study [7] of flow over a wedge, the authors assumed a prescribed power-law profile of the free-stream velocity, which reduces the complexity of the problem too. Moreover, the Reynolds number in most of the earlier studies was rather low.

On the contrary, in the problem examined herein, it is assumed that the porous medium covers only the quarter-plane above the flat plate and does not extend to the space ahead of it. Accordingly, the free-stream velocity does not remain constant but varies in the streamwise direction. The flow is assumed to be maintained by an externally applied forcing which compensates for the resistance of the solid matrix to the motion of fluid.

The flow problem examined herein is relevant to the aerodynamics of bodies with porous surface coatings that can be used for purposes of drag reduction. Another application is flow through emergent vegetation and canopies. An important feature of the boundary-layer profiles in porous media is that they are nonsimilar. More specifically, due to the presence of a characteristic length-scale related to the microstructure of the solid matrix of the porous medium, the governing equations do not admit similarity solutions. This implies that the boundary-layer momentum equation cannot be reduced to an ordinary differential equation (ODE). This is also the case for the flow of interest. It is important to clarify that herein we consider forced but isothermal flow, i.e. in absence of thermal boundary layers. To the author's knowledge, detailed experimental data for this particular setup are currently unavailable.

The paper is structured as follows. In section 2, we present the mathematical formulation of the problem and the parametrization of the resistance from the solid matrix, i.e. the interphasial drag. In section 3 we elaborate on the ODE that governs the free-stream velocity and examine its variation along the streamwise direction. Section 4 contains the derivation the boundary-layer momentum equation in terms of the so-called Görtler transformation[1]. Next, in section 5, we elaborate on the numerical procedures that we employed for the numerical treatment of that equation; these are the local similarity and local nonsimilarity solution methods mentioned above. Then, in section 6 we present numerical results and analyze the structure and properties of the boundary layers of interest. Finally, section 7 concludes.

2 Mathematical formulation

With regard to notation, symbols with a hat, $\hat{\cdot}$, denote dimensional variables, while symbols without a hat denote dimensionless variables. We consider a porous medium of constant porosity ϕ that completely covers the quarter-plane defined by $\hat{x} > 0$ and $\hat{y} > 0$. A solid flat and impermeable plate is located at the boundary of the porous medium at $\hat{y} = 0$. We further consider an incoming stream of fluid with uniform velocity $\hat{u}_0$ at $\hat{x} = 0$ parallel to the flat plate, as shown in figure 1.

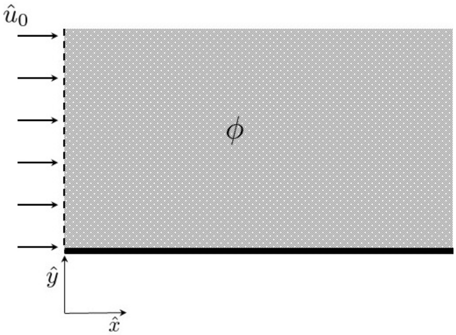

Fig. 1 Schematic representation of the physical problem.

In our study we employ the thermo-mechanical model of [11] for flows in domains partially or fully covered by porous media. This model is based on a mixture-theoretic formalism according to which both the solid matrix and the fluid phase are treated as two distinct, coexisting but immiscible thermodynamic continua [12, 13]. Each phase is endowed with its own set of kinematic and thermodynamic variables and balance laws. Then, the porosity ϕ is introduced as a concentration variable that provides, at each point in space, the volume density (or volume fraction) of the fluid. As such, it satisfies the inequalities, $0 < \phi \leq 1$. The axiomatic definition of the porosity as a density function follows directly from the Radon-Nikodym theorem [14, 15].

Herein, the solid matrix of the porous medium is assumed to consist of non-reacting and rigid fibers at rest; therefore its mass and momentum-balance equations are trivially satisfied. Further, we are concerned with isothermal flow and, therefore, the energy-balance equation for each phase are trivially satisfied too. Then, for steady and constant-density flows, the mass and momentum-balance equations of the fluid read, in dimensional form [16],

$$\nabla \cdot (\hat{\rho}\phi\hat{\boldsymbol{u}}) = 0\,, \tag{1}$$

$$\nabla \cdot (\hat{\rho}\phi\hat{\boldsymbol{u}}\hat{\boldsymbol{u}}) + \phi\nabla\hat{p} = \nabla \cdot \left(\hat{\mu}\phi\hat{\boldsymbol{V}}^{\mathrm{d}}\right) - \hat{\boldsymbol{\delta}}\hat{\boldsymbol{u}}\,. \tag{2}$$

In the above equations, $\hat{\rho}$, $\hat{p}$ and $\hat{\boldsymbol{u}} = (\hat{u}, \hat{v})$ denote the fluid density, dynamic pressure and velocity vector respectively. In the present study, we assume that the flow inside the porous medium is maintained by an externally applied forcing, $\hat{\boldsymbol{F}} = (\hat{F}, 0)$. Therefore, the pressure gradient can be decomposed as follows, $\nabla\hat{p} = -\hat{\boldsymbol{F}} + \nabla\hat{p}'$. Also, $\hat{\mu}$ is the dynamic viscosity of the fluid and $\hat{\boldsymbol{V}}^{\mathrm{d}}$ is twice the deviatoric part of the strain-rate tensor,

$$\hat{\boldsymbol{V}}^{\mathrm{d}} = \nabla\hat{\boldsymbol{u}} + (\nabla\hat{\boldsymbol{u}})^{\top} - \frac{2}{3}(\nabla\cdot\hat{\boldsymbol{u}})\,\boldsymbol{I}\,, \tag{3}$$

with $\boldsymbol{I}$ being the identity matrix. Further, $\hat{\boldsymbol{\delta}}\hat{\boldsymbol{u}}$ represents the interphasial drag force. The drag parameter $\hat{\boldsymbol{\delta}}$ is a second-order tensor since the solid matrix is, in general, an anisotropic medium. An existence and uniqueness theory for the system (1)–(2) has been developed in [17].

In the present study, the fibers that comprise the solid matrix are assumed to be identical circular cylinders of diameter $\hat{d}_{\mathrm{c}}$. Further, these cylindrical elements are considered to be very long, thin and perpendicular to the flat plate. This implies that the solid matrix is an orthotropic medium and, therefore, $\hat{\boldsymbol{\delta}}$ is diagonal. Its diagonal components are denoted by $\hat{\delta}_{11}$ and $\hat{\delta}_{22}$ respectively.

The component $\hat{\delta}_{11}$ is parameterized in the following manner. We consider the expression for the average drag, $\hat{f}_{\mathrm{c}}$, in the horizontal x direction per unit length for a single cylindrical element of the solid matrix. The expression for $\hat{f}_{\mathrm{c}}$ reads,

$$\hat{f}_{\mathrm{c}} = \frac{1}{2}c_{\mathrm{D}}\hat{\rho}\hat{d}_{\mathrm{c}}|\hat{u}|\,\hat{u}\,, \tag{4}$$

where c_D is the bulk drag coefficient for cylinder arrays. In our study, we make use of the following expression for c_D [18, 19],

$$c_{\mathrm{D}} \;=\; 2\left(\frac{\alpha_0}{Re_{\mathrm{c}}} + \alpha_1\right), \tag{5}$$

where $Re_{\mathrm{c}} = \frac{\hat{\rho}\hat{d}_{\mathrm{c}}|\hat{u}|}{\hat{\mu}}$ is the local cylinder-based Reynolds number. In the above equation, α_0 and α_1 are constants that depend on the size of the cylindrical elements and the porosity of the medium. The authors of

The authors of [20] presented correlations for these two parameters based on curve-fitting of experimental data. For sufficiently small cylinders, these correlations reduce to,

$$\alpha_0 \;\approx\; 32\,, \qquad \alpha_1 \;\approx\; 0.5 + 3.2(1-\phi)\,. \tag{6}$$

Other more elaborate expressions for the drag coefficient are available too; see, for example [18–21] and references therein. Nonetheless, in the present study we have opted for the parametrization (5)-(6) due to its simplicity and reasonable accuracy.

The average horizontal force per unit length exerted by the solid matrix is equal to the product of $\hat{f}_{\mathrm{c}}$ and the number of cylinders per unit area, N_{c},

$$N_{\mathrm{c}} \;=\; \frac{4(1-\phi)}{\pi\hat{d}_{\mathrm{c}}^2}\,. \tag{7}$$

By multiplying equations (4) and (7) and by setting the resulting expression equal to $\hat{\delta}_{11}\hat{u}$, we arrive at the following expression for $\hat{\delta}_{11}$,

$$\hat{\delta}_{11} \;=\; \frac{128}{\pi}(1-\phi)\frac{\hat{\mu}}{\hat{d}_{\mathrm{c}}^2} \;+\; \left(2(1-\phi) + 12.8(1-\phi)^2\right)\frac{\hat{\rho}}{\pi\hat{d}_{\mathrm{c}}}|\hat{u}|\,. \tag{8}$$

The parametrization (8) for $\hat{\delta}_{11}$ amounts to a Darcy-Forchheimmer law [2] for the resistance of the solid matrix to fluid motion, in which the permeability is expressed in terms of the porosity and the diameter of the cylindrical elements $\hat{d}_{\mathrm{c}}$. In boundary-layer flows, the momentum equation in the cross-stream direction is automatically satisfied to the first order. Accordingly, the parametrization of $\hat{\delta}_{22}$ is out of the scope of the present study but the interested reader is refer to [11].

For the problem in hand, $\hat{d}_{\mathrm{c}}$ and $\hat{u}_0$ are set as the reference length and velocity, respectively. Then, upon non-dimensionalization of the system of governing equations (1)-(2) and by employing standard scaling arguments, we arrive at the boundary-layer equations for flows in the porous medium of interest,

$$\frac{\partial u}{\partial x} + \frac{\partial v}{\partial y} \;=\; 0\,, \tag{9}$$

$$u\frac{\partial u}{\partial x}+v\frac{\partial u}{\partial y}-F \;=\; \frac{1}{Re_0}\frac{\partial^2 u}{\partial y^2}-\left(bu+cu^2\right), \tag{10}$$

with

$$b \;=\; \frac{128}{\pi Re_0}\,\frac{1-\phi}{\phi}, \quad \text{and} \quad c \;=\; \frac{1}{\pi}\,\frac{2(1-\phi)+12.8(1-\phi)^2}{\phi}. \tag{11}$$

In deriving equations (9), (10) and (11) we have taken into account the fact that the porosity ϕ is constant and that the flow evolves in the positive x direction, i.e. $u > 0$. In the momentum equation (10), F is the only surviving term of the pressure gradient $\nabla\hat{p}$ and represents the external pressure forcing required to maintain the flow in the porous domain; accordingly $F > 0$. Herein we assume that this forcing is constant. Further, in equation (10), Re_0 is the Reynolds number of the incoming stream based on the diameter of the elements of the solid matrix,

$$Re_0 \;=\; \frac{\hat{\rho}\hat{u}_0\hat{d}_{\mathrm{c}}}{\hat{\mu}}. \tag{12}$$

It is worth noting that the difference between the system (9)–(10) and the standard boundary-layer equations for pure-fluid domains is the presence of the forcing term F and the interphasial drag $-(bu + cu^2)$.

Finally, the boundary conditions for the system (9)–(10) read,

$$u(0,y) \;=\; 1, \qquad v(0,y) \;=\; 0, \tag{13}$$

$$u(x,0) \;=\; 0, \qquad v(x,0) \;=\; 0. \tag{14}$$

3 Free-stream velocity

Let u_{e} denote the free-stream velocity in the porous medium, the velocity at the free stream outside the boundary layer. In the free stream, the following relations hold, $v = 0$ and $\frac{\partial u}{\partial y} = 0$. Accordingly, the momentum equation (10) in the free stream reduces to,

$$u_{\mathrm{e}}\frac{\mathrm{d}u_{\mathrm{e}}}{\mathrm{d}x} \;=\; F-\left(bu_{\mathrm{e}}+cu_{\mathrm{e}}^2\right), \tag{15}$$

where F is a positive constant. For a given porosity ϕ and Reynolds number Re_0, the parameters b and c are constant. In this case, (15) becomes a Riccati equation. For $F < b + c$, integration of (15) between 0 and x yields [22],

$$2cx \;=\; \ln\left(\frac{F-(b+c)}{F-(bu_{\mathrm{e}}+cu_{\mathrm{e}}^2)}\right)+\frac{b}{\sqrt{\Delta}}\ln\left(\frac{\sqrt{\Delta}-C(b+2cu_{\mathrm{e}})+2c(1-u_{\mathrm{e}})}{\sqrt{\Delta}-C(b+2cu_{\mathrm{e}})-2c(1-u_{\mathrm{e}})}\right), \tag{16}$$

where $\Delta = b^2 + 4cF$ and $C = \frac{b+2c}{\sqrt{\Delta}}$. For a given x, the above equation can be solved numerically for $u_e(x)$ via an iterative root-finding procedure. Alternatively, equation (15) can be integrated numerically, e.g. via a Runge-Kutta method.

According to (16), as $x \to \infty$, the free-stream velocity u_e converges to its terminal value u_∞,

$$u_\infty = \frac{-b + \sqrt{\Delta}}{2c} < 1\,. \tag{17}$$

In other words, u_∞ is the Darcy-Forchheimer velocity, i.e. the fluid velocity for steady flow in porous media predicted by the Darcy-Forchheimer model. Equation (16) implies that u_e decreases monotonically from $u_e = 1$ at $x = 0$ to u_∞ at $x \to \infty$. Also, according to (17) and for given ϕ and Re_0, the terminal free-stream velocity u_∞ is uniquely determined on the basis of F and vice versa. In the present study we have assumed that $F < b + c$ so that the velocities inside the porous medium are inferior to the velocity of the incoming stream. A reasoning similar to the above holds if one assumes that $F > b + c$, in which case the free-stream velocity exceeds that of the incoming stream.

In general, the decrease of u_e towards u_∞ is rather slow, and it becomes slower as Re_0 increases. This can be directly observed in figure 2 which shows plots of u_e for two different porosities ($\phi = 0.95$ and 0.90 respectively) and four different Reynolds numbers Re_0. In all of these cases, F is such that $u_\infty = 0.25$ according to (17). From these plots we further infer that the decrease rate of u_e becomes substantially larger as the porosity gets smaller. This is a direct consequence of the strong dependence of the interphasial drag on ϕ. Nonetheless, in numerous applications of interest the porosity is quite high, which translates to a slow decrease of u_e even at moderate Re_0. With regard to the numerical integration of the system (9)–(10), this slow decrease of u_e implies that replacing it by its terminal value u_∞ would result in considerable numerical errors even at large distances from the edge of the flat plate.

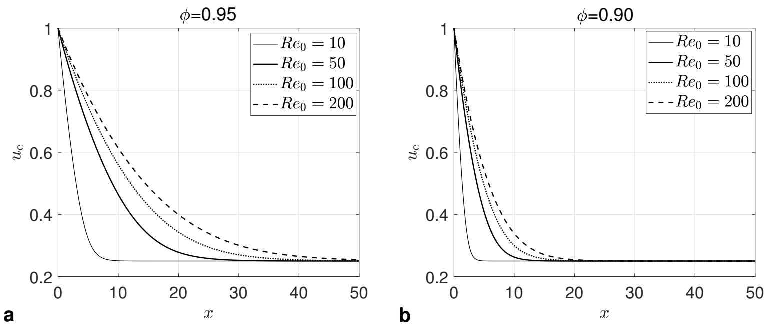

Fig. 2 Plots of the free-stream velocity u_e for four different Reynolds numbers Re_0 and two different porosities ϕ. In the cases shown herein the forcing term F is such that terminal free-stream velocity u_∞ is 1/4 of the velocity of the incoming stream, i.e. is $u_\infty = 0.25$. a) $\phi = 0.95$. b) $\phi = 0.90$.

It is worth adding that at sufficiently small Reynolds numbers, typically $Re_0 \lessapprox 3$, the value of α_1 becomes much smaller than that of the other term in the expression (5) for the drag coefficient c_{D}. Therefore, in this case, α_1 can be neglected and equation (15) reduces to,

$$u_{\mathrm{e}} \frac{\mathrm{d}u_{\mathrm{e}}}{\mathrm{d}x} \;=\; F - b u_{\mathrm{e}}\,, \qquad (Re_0 \lessapprox 3). \tag{18}$$

This is an Abel equation of the first kind [23] and its solution can be obtained by quadrature,

$$u_{\mathrm{e}} \;=\; \grave{u}_\infty \left(1 + W\left(\frac{1}{\grave{u}_\infty} \exp\left(-\frac{bx+k}{\grave{u}_\infty}\right)\right)\right)\,. \tag{19}$$

where W is the Lambert W function [24], and $\grave{u}_\infty = \frac{F}{b}$ is the new terminal value of the free-stream velocity. In fact, $\grave{u}_\infty$ is equal to the Darcy velocity, i.e. the velocity according to Darcy's law for porous-media flows. Further, in (19) k is a constant given by,

$$k \;=\; -(1 - \grave{u}_\infty) + \grave{u}_\infty \ln\left(1 - \grave{u}_\infty\right)\,. \tag{20}$$

The asymptotic approximation of the Lambert W function $W(z)$ for large arguments z reads, $W(z) \approx \ln z - \ln(\ln z) + \frac{\ln(\ln z)}{\ln z}$ [24]. From this expression we may infer that, at large x, u_{e} converges to the terminal value $\grave{u}_\infty$ at a linear rate.

It is noted that, at moderate and high porosities, the coefficient $\frac{1}{Re_0}$ of the viscous-stress term in the full momentum equation is two to three orders of magnitude smaller than the drag coefficient term b whose expression is given in (11). In other words, the ratio of interphasial drag to viscous forces is always high, regardless of the value of Re_0. Accordingly, at moderate and high porosities, the boundary-layer approximation is expected to be valid even at small Reynolds numbers, in the sense that velocity gradients are confined to a layer close to the solid wall.

4 Derivation of the boundary-layer equation for porous media

Following standard procedures, we introduce the so-called Görtler transformation [1, 25], which amounts to the change of variables from (x, y) to (ξ, η) with,

$$\xi \;:=\; \int_0^x u_{\mathrm{e}}(\bar{x})\,\mathrm{d}\bar{x}\,, \qquad \eta \;:=\; u_{\mathrm{e}} y \sqrt{\frac{Re_0}{2\xi}}\,. \tag{21}$$

Then we introduce the stream function Ψ so that the continuity equation (9) is automatically satisfied, i.e. $u = \frac{\partial \Psi}{\partial y}$ and $v = -\frac{\partial \Psi}{\partial x}$. The stream function is thus written in the form,

$$\Psi = \sqrt{\frac{2\xi}{Re_0}}\, f(\xi,\eta)\,. \tag{22}$$

We now introduce the following notation. Differentiation with respect to x or η is denoted by the prime symbol, $u_\mathrm{e}' = \frac{\mathrm{d}u_\mathrm{e}}{\mathrm{d}x}$, $f' = \frac{\partial f}{\partial \eta}$ and so on and so forth. Whereas differentiation with respect to ξ is denoted by $\frac{\partial}{\partial \xi}$. Using this notation, the velocity components are expressed as follows,

$$u = u_\mathrm{e} f'\,, \tag{23}$$

and

$$v = -\sqrt{\frac{2\xi}{Re_0}}\left(\frac{\eta u_\mathrm{e}'}{u_\mathrm{e}} - \frac{\eta u_\mathrm{e}}{2\xi}\right) f' - \left(\frac{f}{\sqrt{2\xi Re_0}} + \sqrt{\frac{2\xi}{Re_0}}\frac{\partial f}{\partial \xi}\right) u_\mathrm{e}\,. \tag{24}$$

Substitution of equations (23) and (24) in the momentum equation (10) leads to the boundary-layer momentum equation for the porous medium of interest,

$$(f''' + ff'') + 2\xi\left(f''\frac{\partial f}{\partial \xi} - f'\frac{\partial f'}{\partial \xi}\right) + \beta_1\left(1 - f'^2\right) + \beta_2\,(1 - f') = 0\,, \tag{25}$$

with

$$\beta_1(\xi) = \frac{2\xi\,(u_\mathrm{e}' + c)}{u_\mathrm{e}^2}\,, \qquad \beta_2(\xi) = \frac{2\xi b}{u_\mathrm{e}^2}\,. \tag{26}$$

On the basis of the coordinate transformation (21), the boundary conditions (13) and (14) translate to the following conditions for f,

$$f(\xi,0) = 0\,, \qquad f'(\xi,0) = 0\,, \qquad f'(\xi,\infty) = 1\,. \tag{27}$$

It is noted that in (25), the contribution of the interphasial drag $-(bu+cu_\mathrm{e}^2)$ is represented in the terms involving β_1 and β_2. Actually, by setting $b = 0$ and $c = 0$ in (26) (no interphasial drag) one recovers the momentum equation for nonsimilar boundary layers in pure-fluid domains [1].

5 Solution method

The boundary-layer momentum equation for porous media (25) can be treated numerically either via implicit finite-difference schemes, such as the Keller's box method [26, 27], or via suitable approximation methods that reduce it to a system of ODEs. Such an approximation method is the Görtler series expansion [1], that assumes a solution of the form $f \approx \sum_n \xi^n g_n(\eta)$. By inserting this ansatz into (25) one obtains a system of coupled ODEs (one equation for each g_n) that can be solved sequentially. This method has been successfully applied when the function β_1 can be expanded in a power series of ξ. Relevant examples include flows over a curved plate and flows with an adverse pressure gradient [1].

In the context of the present study, we tested a three-term expansion, i.e. $f \approx g_0(\eta) + \xi g_1(\eta) + \xi^2 g_2(\eta)$, while using the full expression (26) for β_1. However, this approach did not result in numerically converged results. More specifically, this expansion did not yield monotonic profiles even at small Reynolds numbers Re_0. This is attributed to the presence of the term $\beta_2\,(1 - f')$ in (25) and, possibly, to complexities related to the representation of u_e and its derivative.

For this reason, in the present study we opted for the local nonsimilarity solution method of Sparrow et al. [6]. The advantages of this approach are conceptual simplicity and straightforward implementation. The authors of [6] reported good agreement of the predictions of their approach with those of finite-difference methods for various nonsimilar boundary layers in pure-fluid domains, such as Howarth's retarded flow, cylinder in cross flow and flat plate with mass injection. Since its development, this approach has been successfully employed for the computation of nonsimilar boundary layers, including those in porous domains [7, 9, 10]. It is worth adding that, in their study of flow over a wedge embedded in a porous domain, the authors of [7] reported good agreement between the predictions of local nonsimilarity, finite difference and series expansion methods.

Below we present the application of the local nonsimilarity approach in the numerical integration of (25). The underlying idea of this method is that in boundary-layer flows the velocity gradients in the cross-flow direction y are typically larger than those in the flow direction x. It is therefore expected that the derivatives of f with respect to η are considerably larger than those with respect to ξ.

Accordingly, at the first level of truncation, one may neglect the terms involving partial derivatives with respect to ξ in (25). This results in the so-called *local similarity* model, referred to herein as LS,

$$f''' + f f'' + \beta_1 \left(1 - {f'}^2\right) + \beta_2\,(1 - f') \;=\; 0\,, \tag{28}$$

with boundary conditions given by (27). In this manner, however, a part of the boundary-layer momentum equation is lost.

According to the local nonsimilarity method [6], and in order to alleviate the error of the local similarity model (28), one defines,

$$g \;:=\; \frac{\partial f}{\partial \xi}\,, \tag{29}$$

and differentiates (25) with respect to ξ. This yields the equation,

$$g''' + fg'' - 2\,(\beta_1 + 1)\, f'g' - \beta_2 g' + 3f''g + \frac{\mathrm{d}\beta_1}{\mathrm{d}\xi}\left(1 - f'^2\right) + \frac{\mathrm{d}\beta_2}{\mathrm{d}\xi}\,(1 - f') + 2\xi\frac{\partial}{\partial\xi}\,(f''g - f'g') \;=\; 0\,. \tag{30}$$

Additionally, the boundary conditions (27) are also differentiated with respect to ξ.

Then, at the second level of truncation, terms in (30) involving partial derivatives with respect to ξ are neglected, while retaining the full boundary-layer momentum equation (25) with g being treated as a new unknown variable. This leads to the following local-nonsimilarity model, referred to herein as LNS1,

$$\left\{\begin{aligned} & f''' + ff'' + 2\xi\,(f''g - f'g') + \beta_1\left(1 - f'^2\right) + \beta_2\,(1 - f') \;=\; 0\,, && (31)\\ & g''' + fg'' - 2\,(\beta_1 + 1)\, f'g' - \beta_2 g' + 3f''g + \frac{\mathrm{d}\beta_1}{\mathrm{d}\xi}\left(1 - f'^2\right) + \\ & \frac{\mathrm{d}\beta_2}{\mathrm{d}\xi}\,(1 - f') \;=\; 0\,, && (32)\end{aligned}\right.$$

with boundary conditions,

$$f(\xi,0) \;=\; g(\xi,0) \;=\; 0\,, \qquad f'(\xi,0) \;=\; g'(\xi,0) \;=\; 0\,, \tag{33}$$

$$f'(\xi,\infty) \;=\; 1\,, \qquad g'(\xi,\infty) \;=\; 0\,. \tag{34}$$

In other words, LNS1 consists of the coupled system of ODEs (31)-(32) for the vector of unknowns (f, g).

In order to improve the accuracy of the computations, one can introduce a third level of truncation. To this end, one defines,

$$h \;:=\; \frac{\partial g}{\partial \xi}\,, \tag{35}$$

and differentiates (30) with respect to ξ along with its boundary conditions. This leads to a new equation involving f, g, h and their derivatives. Then, in this new equation, partial derivatives with respect to ξ are neglected and the resulting ODE is combined with the full equations (25) and (30). This procedure results in an improved local nonsimilarity model, referred to herein as LNS2,

$$\begin{cases} f''' + ff'' + 2\xi\,(f''g - f'g') + \beta_1\left(1 - f'^2\right) + \beta_2\,(1 - f') \;=\; 0\,, & (36)\\[2ex] g''' + fg'' - 2\,(\beta_1 + 1)\,f'g' - \beta_2 g' + 3f''g + \dfrac{\mathrm{d}\beta_1}{\mathrm{d}\xi}\left(1 - f'^2\right) + \\ \dfrac{\mathrm{d}\beta_2}{\mathrm{d}\xi}\,(1 - f') - 2\xi\left(g'^2 - gg'' + f'h' - f''h\right) \;=\; 0\,, & (37)\\[2ex] h''' + fh'' - 2\,(\beta_1 + 2)\left(g'^2 + f'h'\right) - \beta_2 h' - 5f''h + 6gg'' \\ -4\dfrac{\mathrm{d}\beta_1}{\mathrm{d}\xi}f'g' - 2\dfrac{\mathrm{d}\beta_2}{\mathrm{d}\xi}g' \;=\; 0\,. & (38) \end{cases}$$

with boundary conditions,

$$f(\xi,0) \;=\; g(\xi,0) \;=\; h(\xi,0) \;=\; 0\,, \quad f'(\xi,0) \;=\; g'(\xi,0) \;=\; h'(\xi,0) \;=\; 0\,, \tag{39}$$

$$f'(\xi,\infty) \;=\; 1\,, \qquad g'(\xi,\infty) \;=\; h'(\xi,\infty) \;=\; 0\,. \tag{40}$$

In other words, LNS2 consists of the coupled system of ODEs (36)-(38) for the vector of unknowns (f, g, h).

By proceeding in this manner, one can derive a sequence of coupled ODEs that are meant to approximate the boundary-layer momentum equation (25) to an increasing degree of accuracy. Typically though, the solution method based on the third level of truncation provides a satisfactory level of accuracy, as shown in the examples of [6].

With regard to computational procedures, the local similarity model LS (28) can be integrated numerically with standard algorithms for boundary-value problems [28]. In our study, we successfully employed the simple shooting method for values of ξ as high as $\xi = 80$.

On the other hand, the numerical integration of the local nonsimilarity models LNS1 and LNS2, (31)–(32) and (36)-(37) respectively, requires a little more care because simple shooting does not always yield converged results for large values of ξ. One approach is to integrate these systems via a multiple-shooting method [28] which is more robust than simple shooting. However, such a method is cumbersome to implement, especially for highly nonlinear systems such as (31)–(32) and (36)-(37), and computationally rather expensive.

For this reason we have opted for the approach proposed in [6] which is simple to implement and quite efficient. According to it, one performs the numerical integration of the system of interest from 0 to $\eta_{\max}$ via simple shooting. Initially, $\eta_{\max}$ is assigned a small value so that simple shooting can easily yield a converged solution. Then, the value of $\eta_{\max}$ is progressively increased until the pre-assigned tolerances on the computation of the dependent variables are met.

Numerical tests that we conducted for ξ up to $\xi = 80$, showed that this approach is indeed well adapted for the models LNS1 and LNS2, (31)–(32) and (36)-(37) respectively. In the present study, for each $\eta_{\max}$, these systems have been integrated from 0 to $\eta_{\max}$ via a simple shooting method using the l^2 norm of the solution vector, (f, g) or (f, g, h), in the numerical-convergence criterion. In our computations, convergence was assumed when the difference between the norms of successive approximations became less than 10^{-5}. During each iteration step of the shooting method, the ODEs were solved via a 4th-order Runge-Kutta scheme. According to our numerical tests, for Reynolds numbers up to $Re_0 = 200$, the value $\eta_{\max} = 5$ (or smaller) was a very good approximation of $\eta \to \infty$, in the sense that the boundary conditions at $\eta \to \infty$ were satisfied at $\eta_{\max} = 5$ within the preassigned accuracy of the numerical integration of the ODEs.

It is worth adding that an alternative approach for the numerical treatment of nonsimilar boundary layers is the homotopy analysis method [29] which yields a convergent series expansion of the sought-after solution. Nonetheless, in the present study we have opted for the local nonsimilarity method of [6] due to its simplicity and straightforward implementation.

6 Numerical results

In the framework of our study, we have computed numerical solutions of (25), via the local similarity and local nonsimilarity methods, for a variety of Reynolds numbers Re_0 and porosities ϕ. A sample of the numerical results that we obtained is presented below. Unless otherwise mentioned, the porosity of the medium is set at $\phi = 0.95$, the Reynolds number at $Re_0 = 50$ and the external forcing F to a value such that the terminal free-stream velocity is $u_\infty = 0.25$.

In figure 3 we present velocity profiles at different distances from the edge of the flat plate, computed with the nonsimilarity method LNS2. According to these plots, the velocity increases quite rapidly with y and reaches the free-stream value u_e within a few unit lengths above the flat plate. Further, at a certain distance from the edge of the flat plate, $x \approx 30$, the free-stream velocity u_e has almost converged to its terminal value u_∞; see also figure 2a for $Re_0 = 50$. Beyond this distance, the profile of u_e is stabilized and no longer evolves with the streamwise distance x.

For comparison purposes, in Figure 4 we present plots of the velocity profile at $x = 10$ computed with the three methods described above, namely, the local similarity model LS (28) and the local nonsimilarity models LNS1 (31)–(32) and LNS2 (36)–(38). From this figure we can observe that the three profiles are quite close to one another. The model with the lowest accuracy, LS, provides a reasonable approximation of the velocity profile. Moreover, the difference between the profiles computed with LNS1 and LNS2 is barely discernible. In Figure 4b, we show a zoom of the numerically computed profiles in the interval $0.35 \leq y \leq 0.45$, which is the region where these profiles differ

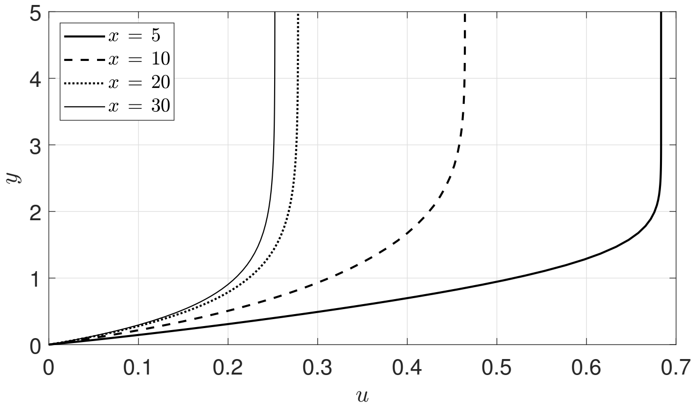

Fig. 3 Velocity profiles at different distances from the edge of the flat plate. $\phi = 0.95$, $Re_0 = 50$, and $u_\infty = 0.25$.

the most. Therein we readily observe that the difference between the profiles computed via LS and LNS1 is already small, whereas the difference between the LNS1 and LNS2 profiles is still much smaller. This serves as an indication that the sequence of nonsimilarity models proposed in [6] does in fact lead to numerically converged solutions.

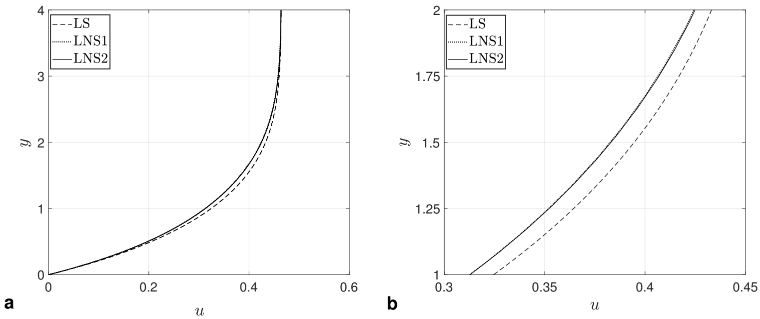

Fig. 4 a) Velocity profiles at $x = 10$ (for $\phi = 0.95$, $Re_0 = 50$ and $u_\infty = 0.25$) computed with the local similarity method LS (28) and the local nonsimilarity models LNS1 (31)–(32) and LNS2 (36)–(38). (b) Zoom of the profiles in the interval $0.30 \leq y \leq 0.45$.

One quantity of particular interest is the shear stress at the wall $\hat{\tau}_\mathrm{w}$. For flows in porous domains this is defined as

$$\hat{\tau}_\mathrm{w} = \phi \hat{\mu} \left(\frac{\partial \hat{u}}{\partial \hat{y}} \right)_{\hat{y}=0} . \tag{41}$$

We now insert (23) into (41) and carry out the differentiation with respect to y by using the chain rule and the change of variables (21). In this manner, we obtain the following expression for τ_{w}, non-dimensionalized by $\hat{\rho}\hat{u}_0^2$,

$$\tau_{\mathrm{w}} = \frac{\phi u_{\mathrm{e}}^2}{\sqrt{2\xi Re_0}} f''(\xi, 0) \,. \tag{42}$$

Typically, the dimensional wall stress is cast in terms of the friction factor c_{f}, $\hat{\tau}_{\mathrm{w}} = \frac{1}{2} c_{\mathrm{f}} \hat{\rho}\hat{u}_0^2$. Therefore, the dimensionless wall stress given above is equal to one half of the friction factor, $\tau_{\mathrm{w}} = \frac{1}{2} c_{\mathrm{f}}$.

In figure 5 we provide plots of the profiles of τ_{w} computed with the local similarity model LS and the local nonsimilarity models LNS1 and LNS2. We can observe that τ_{w} decreases monotonically with the distance x from the edge of the flat plate and eventually reaches an asymptotic value as the free-stream velocity u_{e} approaches its terminal value u_∞. Evidently, this is due to the fact that, in the far field, the velocity profile no longer varies with x. By comparing the plots computed with the three solution methods we readily infer that the local similarity approximation LS yields reasonably accurate results. The local nonsimilarity model LNS1 yields mildly improved results with respect to those obtained with LS. Whereas the results obtained with LNS1 and LNS2 are practically identical.

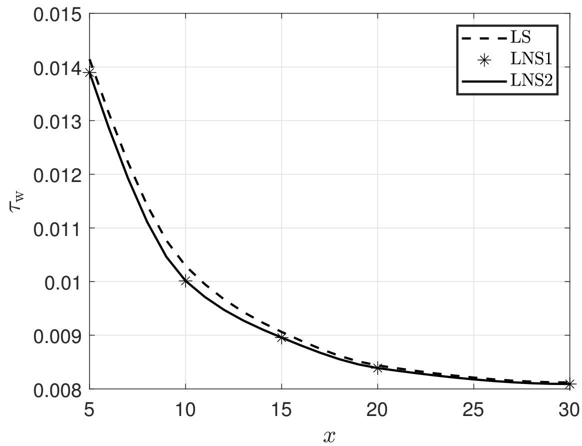

Fig. 5 Wall-stress profiles (for $\phi = 0.95$, $Re_0 = 50$ and $u_\infty = 0.25$) computed with the local similarity, LS, and the local nonsimilarity models LNS1 and LNS2.

We may therefore infer that in terms of numerical accuracy, ease of implementation and computational cost, the local nonsimilarity model NLS1 is the most advantageous option for computing the boundary layers of interest.

Another interesting quantity is the boundary-layer thickness δ. This is defined as the height (y coordinate) at which the streamwise velocity u reaches 99% of the value of the free-stream u_{e} at this location. Plots of δ for four different cases are provided in figure 6. From this figure we infer that, overall, δ is quite thin and at the order of a few unit lengths, i.e. a few cylinder diameters. Moreover, by comparing the profiles for the different cases shown therein, we deduce that an increase of Re_0 (higher incoming velocity) results in a decrease of δ. Similarly, δ decreases as the forcing F (hence the terminal free-stream velocity u_∞) increases.

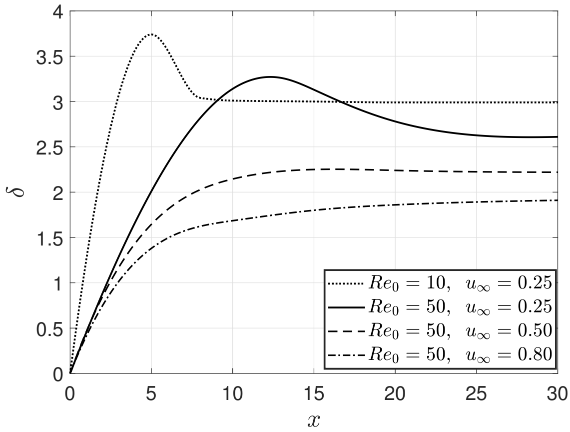

Fig. 6 Profiles of the boundary-layer thickness δ for three different cases. In all cases, the porosity is set at $\phi = 0.95$.

An interesting feature is that, in certain cases, δ increases rapidly close to the edge of the flat plate and then reaches a peak value at some distance downstream. Beyond the location of this peak, δ decreases and converges to a terminal value as $u_\mathrm{e} \to u_\infty$. This trend has been observed when the terminal free-stream velocity u_∞ is small. For example, in figure 6 the overshoot of δ is quite pronounced when $u_\infty = 0.25$ but is barely discernible when $u_\infty = 0.5$. On the other hand, when $u_\infty = 0.80$, δ increases monotonically and converges to an asymptotic value far downstream.

Our computations further showed that the profile of the displacement thickness follows the same trend as well, depending on the value of u_∞. It is worth adding that the peak and subsequent decrease of δ for small u_∞ has been predicted by all solution methods, including the local similarity one LS. Therefore, this peak is not related to terms of the momentum equation (25) involving partial derivatives of f with respect to ξ.

In fact, the overshoot of δ is related to the change of sign of β_1, *cf.* (25), which in turn is controlled by $u_\mathrm{e}'(x)$. More specifically, from (26) we deduce that β_1 changes sign when $u_\mathrm{e}' = -c$. Then, by substituting this value of u_e' in (15), we observe that the change of sign of β_1 occurs when u_e attains the following critical value u_cr,

$$u_\mathrm{cr} = \frac{F}{b} \,. \tag{43}$$

According to this equation, $u_{\rm cr}$ increases as F increases. By virtue of (17), this implies that $u_{\rm cr}$ increases as u_∞ increases. Further, from (17) and (43), we readily deduce that $u_{\rm cr} > u_\infty$, whereas $u_{\rm cr}$ can be either larger or smaller to the velocity of the incoming stream.

When F hence u_∞ are sufficiently small, then $u_\infty < u_{\rm cr} < 1$, *i.e.* the critical value is lower than the velocity of the incoming stream. Accordingly, at small x, the free-stream velocity $u_{\rm e}$ decreases rapidly and $u_{\rm e}'$ takes large negative values so that β_1 is negative. But at a given distance, $u_{\rm e}$ becomes equal to $u_{\rm cr}$. This means that the magnitude of $u_{\rm e}'$ has decreased to the point that β_1 changes sign from positive to negative. This case corresponds to an overshoot of the boundary layer thickness δ.

On the other hand, when F hence u_∞ are large, then $u_{\rm cr} > 1 > u_\infty$. In this case, the free-stream velocity $u_{\rm e}$ remains smaller than the critical value $u_{\rm cr}$. Then $u_{\rm e}$ decreases slowly towards u_∞ and the magnitude of $u_{\rm e}'$ is kept small so that β_1 remains always positive. This case corresponds to a monotonically increasing boundary-layer thickness δ.

The above analysis has been corroborated by our numerical computations. In the particular example considered herein, $\phi = 0.95$ and $Re_0 = 50$, the critical velocity $u_{\rm cr}$ becomes equal to unity for $u_\infty = 0.615$. Accordingly, for $u_\infty < 0.615$ there is an overshoot in δ, whereas for $u_\infty > 0.615$ the thickness δ increases monotonically. This can be readily confirmed from the plots of figure 6 according to which the profile of δ exhibits overshoots for $u_\infty = 0.25$, 0.50 but is monotonic for $u_\infty = 0.80$.

From the above discussion, it becomes evident that the overshoot of the boundary-layer thickness is due to the interphasial drag; in other words, it is a unique feature of porous media and is not encountered in equivalent flows in pure-fluid domains.

7 Conclusions

In the present paper we have examined the structure of the boundary-layer flow that is developed when a uniform stream of fluid enters a porous domain located above a flat plate. The flow in the porous medium is maintained by a constant external pressure forcing. Such boundary layers are nonsimilar, which is explained by the presence of a characteristic length-scale, namely, the size of the elements that comprise the solid matrix of the porous medium. In our study the solid matrix is assumed to consist of identical and vertically aligned cylindrical elements. The drag force experienced by the cylindrical elements is given in terms of a Darcy-Forchheimer law. The resulting momentum boundary-layer equation is then solved using the local similarity and two local nonsimilarity methods. The basic assumption of the local nonsimilarity approach is that the solution varies sufficiently smoothly in the streamwise direction so that the boundary-layer momentum equation (25) can be approximated by a sequence of ODEs.

According to our numerical tests, and for the boundary layers of interest, the local similarity method gives fairly accurate results. The first local nonsimilarity method, which is based on a second level of truncation of the momentum equation, provides improved results. Whereas the second local nonsimilarity method, which uses a third level of truncation, yields results that are almost identical to those of the first one.

Our computations showed that the free-stream velocity u_{e} decreases monotonically towards a terminal value u_{∞}. In general, the rate of decrease of the free-stream velocity is significant near the edge of the flat plate but then it becomes smaller further downstream. The decrease rate of u_{e} attenuates when the Reynolds number or the external pressure forcing F increase. Once u_{e} reaches its terminal value u_{∞}, then the velocity profile stabilizes and ceases to vary in the streamwise direction.

In general, the thickness of the layers is at the order of a few diameters of the cylindrical elements of the solid matrix. An interesting feature is that for sufficiently low terminal free-stream velocities, i.e small external pressure forcing, the boundary-layer thickness exhibits an overshoot and then decreases towards its terminal value. This is attributed to the large variation of the slope of the free-stream velocity u_{e} which results in the change of sign of a term in the boundary-layer equation (25). On the other hand, the wall stress always decreases monotonically in the streamwise direction.

Finally, it is worth adding that while in the numerical study presented herein we assumed that the external forcing F is constant, one may envisage cases where F varies along the streamwise direction. In such cases, it is expected that the local nonsimilarity approach will still be applicable, provided that F is varies sufficiently slowly so that the free-stream velocity, which is linked with F via (15), varies slowly too.

- **Funding** No funding was received for conducting this study.
- **Conflict of interest** The author has no competing interests to declare that are relevant to the content of this article.

References

[1] Schlichting, H., Gersten, K.: Boundary-Layer Theory, 9th edn. Springer, Berlin (2017)

[2] Nield, D.A., Bejan, A.: Convection in Porous Media, 5th edn. Springer, New York (2017)

[3] Vafai, K., Tien, C.L.: Boundary and inertial effects on flow and heat transfer in porous media. Int. J. Heat Mass Tran. **24**, 195–203 (1981)

[4] Vafai, K., Thiyagaraja, R.: Analysis of flow and heat transfer at the interface region of a porous medium. Int. J. Heat Mass Tran. **2304**, 1391–1405 (1987)

[5] Nakayama, A., Kokudai, T., Koyama, H.: Non-Darcian boundary layer flow and forced convective heat transfer over a flat plate in a fluid-saturated porous medium. J. Heat Tran. **112**, 157–162 (1990)

[6] Sparrow, E.M., Quack, H., Boerner, C.J.: Local nonsimilarity boundary-layer solutions. AIAA J. **8**, 1936–1942 (1970)

[7] Hossain, M.A., Banu, N., Nakayama, A.: Non-Darcy forced convection boundary layer flow over a wedge embedded in a saturated porous medium. Numer. Heat Tr. A - Appl. **26**, 399–414 (1994)

[8] Qawasmeh, B.R., Alrbrai, M., Al-Dahidi, S.: Forced convection heat transfer of Casson fluid in non-Darcy porous media. Int. Comm. Heat Mass **11**, 1–10 (2019)

[9] Farooq, U., Ijaz, M.A., Khan, M.I., Isa, S.S.P.M., Lu, D.C.: Modeling and non-similar analysis for Darcy-Forchheimer-Brinkman model of Casson fluid in a porous media. Int. Comm. Heat Mass **119**, 104955 (2020)

[10] Farooq, U., Hussain, M., Ijaz, M.A., Khan, W.A., Farooq, F.B.: Impact of non-similar modeling on Darcy-Forchheimer-Brinkman model for forced convection of Casson nano-fluid in non-Darcy porous media. Int. Comm. Heat Mass **125**, 105312 (2021)

[11] Papalexandris, M.V., Antoniadis, P.D.: A thermo-mechanical model for flows in superposed porous and fluid layers with interphasial heat and mass exchange. Int. J. Heat Mass Tran. **88**, 42–54 (2015)

[12] Straughan, B.: Stability and Wave Motion in Porous Media. Springer, New York (2008)

[13] Cowin, S.C.: Continuum Mechanics of Anisotropic Materials. Springer, New York (2013)

[14] A.Goodman, M., Cowin, S.C.: A continuum theory for granular materials. Arch. Rat. Mech. Anal. **44**, 249–266 (1972)

[15] Varsakelis, C., Papalexandris, M.V.: The equilibrium limit of a constitutive model for two-phase granular mixtures and its numerical approximation. J. Comp. Phys. **229**, 4183–4207 (2010)

[16] Antoniadis, P.D., Papalexandris, M.V.: Dynamics of shear layers at the interface of a highly porous medium and a pure fluid. Phys. Fluids **27**, 014104 (2015)

[17] Varsakelis, C., Papalexandris, M.V.: On the well-posedness of the Darcy–Brinkman–Forchheimer equations for coupled porous media-clear

fluid flow. Nonlinearity **30**, 1449–1464 (2017)

[18] Tanino, Y., Nepf, H.M.: Laboratory investigation of mean drag in a random array of rigid, emergent cylinders. J. Hydraul. Eng. **134**, 534–41 (2008)

[19] Tinoco, R.O., Cowen, E.A.: The direct and indirect measurement of boundary stress and drag on individual and complex arrays of elements. Exp. Fluids **54**, 1–16 (2013)

[20] Sonnenwald, F., Stovin, V.R., Guymer, I.: Estimating drag coefficient for arrays of rigid cylinders representing emergent vegetation. J. Hydraul. Res. **57**, 591–597 (2019)

[21] Koch, D.L., Ladd, A.J.C.: Moderate Reynolds number flows through periodic and random arrays of aligned cylinders. J. Fluid Mech. **349**, 31–66 (1997)

[22] Gradshteyn, I.S., Ryzhik, I.M.: Tables of Integrals, Series, and Products, 5th edn. Academic Press, San Diego, CA (1994)

[23] Polyamin, A.D., Zaitsev, V.F.: Handbook of Exact Solutions of Ordinary Differential Equations. CRC Press, Boca Raton, FL (1995)

[24] Corless, R.M., Gonnet, G.H., Hare, D.E.G., Jeffrey, D.J., Knuth, D.E.: On the Lambert W function. Adv. Comput. Math. **5**, 329–359 (1996)

[25] Görtler, H.: A new series for the calculation of steady laminar boundary layers. J. Math. Mech. **6**, 1–66 (1957)

[26] Keller, H.: A new difference scheme for parabolic problems. In: Bramble, J. (ed.) Numerical Solution of Partial Differential Equations, Vol. II. Academic Press, San Diego, CA (1970)

[27] Cebeci, T.: Modeling and Computation of Boundary-Layer Flows. Springer, New York (2005)

[28] Stoer, J., Bulirsch, R.: Introduction to Numerical Analysis. Springer, New York (1993)

[29] Liao, S.J.: A general approach to get series solution of non-similarity boundary-layer flows. Commun. Nonlinear Sci. **14**, 2144–2159 (2009)